Direct numerical simulations of two-phase flow in an inclined pipe

Fangfang Xie[1,2]**, Xiaoning Zheng**[3]**, Michael S. Triantafyllou**[2,†]**,
Yiannis Constantinides**[4]**, Yao Zheng**[1]** and George Em Karniadakis**[3]

[1]School of Aeronautics and Astronautics, Zhejiang University, Hangzhou, ZJ 310027, China

[2]Department of Mechanical Engineering, Massachusetts Institute Technology, Cambridge, MA 02139, USA

[3]Division of Applied Mathematics, Brown University, Providence, RI 02912, USA

[4]Chevron Energy Technology Company, Houston, TX 77002, USA

We study the instability mechanisms leading to slug flow formation in an inclined pipe subject to gravity forces. We use a phase-field approach, where the Cahn–Hillard model is used to model the interface. At the inlet, a stratified flow is imposed with a specified velocity profile. We validate our numerical results by comparing against previous theoretical models and by predicting the various flow regimes for horizontal and inclined pipes, including stratified flow, slug flow, dispersed bubble flow and annular flow. Subsequently, we focus on slug formation in an inclined pipe and connect its appearance with specific vortical dynamics. A two-dimensional channel geometry is first considered. When the heavy fluid is injected as the top layer, inverted vortex shedding emerges, which periodically impacts on the bottom wall, as it develops further downstream. The accumulation of heavy fluid in the bottom wall causes a back flow that induces rolling waves and interacts with the upstream jet. When the heavy fluid is placed as the bottom layer, the heavy fluid accumulates and initially forms a massive slug at the bottom region, close to the inlet. Subsequently, the heavy fluid slug starts to break into smaller pieces, some of which translate along the pipe. During the accumulation phase, a back flow forms also generating rolling waves. Occasionally, a rolling wave can reach the top of the pipe and form a new slug. To describe the generation of vorticity from the two-phase interface and pipe walls in the slug formation, we study the circulation dynamics and connect it with the resulting two-phase flow patterns. Finally, we conduct three-dimensional (3-D) simulations in a circular pipe and compare the differences between the 3-D flow patterns and its circulation dynamics against the 2-D simulation results.

Key words: gas/liquid flows, instability, multiphase and particle-laden flows

1. Introduction

Transportation of two-phase flow through pipelines is used often in industrial applications, such as in the oil and gas industry and in offshore engineering.

† Email address for correspondence: mistetri@mit.edu

Depending on the governing parameters of the problem, a wide range of flow regimes may be encountered, with complex and dynamic interfacial topologies, including bubbly flow, plug flow, slug flow, stratified flow and annular flow (Taitel & Dukler 1976; Shoham 2006; Campbell 2015).

The slug flow is a commonly encountered flow regime in pipelines of the oil industry (Sausen, de Campos & Sausen 2012). It is characterized by a highly intermittent flow, in which large gas bubbles flow alternatively with liquid slugs, with a randomly fluctuating frequency (Fabre & Liné 1992). The presence of slugs can cause severe dynamic problems by creating pressure transients, leading to flooding at the receiving end or increased deposits and corrosion (Bratland 2010). Therefore, understanding the hydrodynamic properties of slug flow mechanics is of great importance to oil and gas engineers for the design and flow assurance of pipelines.

Although a large number of theoretical studies have been conducted investigating the slug flow patterns and their characteristics, such as the 'unit-cell' approach (Dukler & Hubbard 1975; Taitel & Barnea 1990), slug-tracking model (Bendiksen *et al.* 1990; Barnea & Taitel 1993; Zheng, Brill & Taitel 1994) and slug capturing technique (Issa & Kempf 2003), an accurate simulation under realistic flow conditions is not available yet. Computational fluid dynamics (CFD) proves to be a very attractive alternative. Two-phase direct numerical simulations (DNS) have been employed to study bubbly flows (Esmaeeli & Tryggvason 1998, 1999; Bunner & Tryggvason 2002*a*,*b*; Nagrath, Jansen & Lahey 2005). However, DNS results for other flow regimes are very rare.

Pipelines that connect wells on the seabed to production platforms are usually installed on irregular bottom topographies, so that the pipeline system normally contains combinations of several uphill and downhill sections, as well as curving bends. It is found that stratified flow may appear in the downward sections, while a slug flow could be triggered in the horizontal and upward sections with high probability (Sanchez-Silva *et al.* 2013). Therefore, DNS of two-phase flow in an inclined pipe is the focus in the current study. We start out by considering a stratified flow under the effect of gravity; then we investigate the instability mechanisms of two-phase flow and, especially, the slug formation principles.

Vorticity dynamics has proved useful in illustrating the physics of fluid flow (Rosenhead 1963; Morton 1984; Batchelor 2000), including the generation and redistribution of vorticity. For two-phase flow in an inclined pipe, the sources of vorticity generation are the solid boundaries and the interfaces between the two fluids. In single-phase fluid, vorticity is generated at the walls; in two-dimensional (2-D) steady channel flow (plane Poiseuille flow) for example, vorticity generated at the top wall is equal and of opposite sign than the vorticity generated on the bottom wall (Morton 1984); the vorticity source can be identified by calculating the pressure gradient. In a fluid–fluid interface, vorticity is generated mainly from its normal motion when the interface is curved and there is non-zero tangential motion (Brøns *et al.* 2014). In the present work, circulation dynamics is used to quantitatively analyse the amount of vorticity generation at various locations, where special flow structures might emerge.

The paper is organized as follows. In §2, the numerical algorithm for two-phase flow is described and a validation against previous theoretical models is carried out. In §3, the instability mechanisms of two-phase flow in the 2-D upward inclined pipe are first discussed. The effect of inflow condition and inclination angle on the flow transition, vorticity generation and circulation dynamics are investigated. In §4, three-dimensional simulations in a circular pipe are conducted and the results are compared against those of 2-D simulations. Finally, in §5 we provide the final conclusions.

2. Problem formulation and numerical method

2.1. *Numerical method*

To track the interface between two fluids and capture the high-order approximations of interfacial dynamics, a phase-field approach is applied in our study (Dong & Shen 2012).

Compared to other interface-capturing methods, such as the front tracking (Tryggvason *et al.* 2001), level set (Sussman, Smereka & Osher 1994) and volume-of-fluid (VOF) (Hirt & Nichols 1981) approaches, the phase-field approach exhibits several advantages. First, it is a physically motivated method and the Cahn–Hillard model describes the interface by a mixing energy formulation. Second, it can easily handle topological changes since the formulations are performed on a fixed grid in Eulerian framework. In addition, it can solve the moving contact line problem due to the diffuse interface involved.

The two-phase flow with the phase-field approach (Dong & Shen 2012) is described by the following system of coupled equations:

$$\rho \left(\frac{\partial \boldsymbol{u}}{\partial t} + \boldsymbol{u} \cdot \nabla \boldsymbol{u} \right) = -\nabla p + \nabla \cdot [\mu (\nabla \boldsymbol{u} + \nabla \boldsymbol{u}^{\mathrm{T}})] - \lambda \nabla \cdot (\nabla \phi \nabla \phi) + \boldsymbol{g}(\boldsymbol{x}, t), \quad (2.1a)$$

$$\nabla \cdot \boldsymbol{u} = 0, \quad (2.1b)$$

$$\frac{\partial \phi}{\partial t} + \boldsymbol{u} \cdot \nabla \phi = -\lambda \gamma_1 \nabla^2 [\nabla^2 \phi - h(\phi)]. \quad (2.1c)$$

In the above set of equations, (2.1a) is the Navier–Stokes equation, (2.1b) is the continuity equation, while (2.1c) is the Cahn–Hilliard equation.

Here, $\boldsymbol{u}(\boldsymbol{x}, t)$ is the velocity, $p(\boldsymbol{x}, t)$ is the pressure, $\boldsymbol{g}(\boldsymbol{x}, t)$ is a body force (such as gravity). $\phi(\boldsymbol{x}, t)$ is the phase-field function, where $-1 \leqslant \phi \leqslant 1$. The flow regions with $\phi = 1$ and $\phi = -1$ represent the first fluid and the second fluid, respectively. The iso-surface $\phi(\boldsymbol{x}, t) = 0$ marks the interface between the two fluids at time t, while $h(\phi)$ is given by $h(\phi) = 1/\eta^2 \phi(\phi^2 - 1)$ and η is a characteristic length scale of the interface thickness. γ_1 is the mobility of the interface, and is assumed to be constant. λ is the mixing energy density coefficient and is related to the surface tension σ by Yue *et al.* (2004). There is a diffusion term $(\nabla^2 \phi - h(\phi))$ on the right-hand side of (2.1c), which is different from corresponding terms in the VOF or the level set function methods. This diffusion term $(\nabla^2 \phi - h(\phi))$ is the gradient of the mixing energy density W, where $W = \int_{\Omega} (\lambda/2 |\nabla \phi|^2 + \lambda/4/\eta^2 (\phi^2 - 1)^2) \, \mathrm{d}\Omega$. The first term of the integrand tends to mix the two fluids so that the gradient will approach zero when energy is minimized; the second term (double-well potential) of the integrand tends to separate the two fluids. The interplay between these two tendencies will determine the dynamic profile of the interface, see Yue *et al.* (2004). One can refer to Dong & Shen (2012) for more details of these parameters. Moreover, the non-dimensional form for the flow variables and physical parameters can be found in Zheng *et al.* (2015).

The above two-phase system is solved by the parallelized code Nektar, based on the spectral/hp element method (Karniadakis & Sherwin 2013). This version of the code employs a splitting scheme as a decoupling strategy to efficiently solve the system of partial differential equations (PDEs) obtained from phase-field formulation. Details regarding time integration schemes and validation studies of the numerical method and parameters have been reported in Dong & Shen (2012), Zheng & Karniadakis (2016).
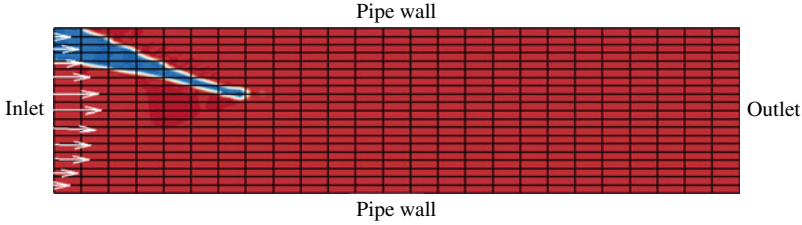
FIGURE 1. (Colour online) Initial simulation set-up for the pipe conveying two-phase flow. The spectral element mesh (medium resolution) is shown in the background. Red denotes the light fluid and blue denotes the heavy fluid.

2.2. *Simulation set-up*

As seen from figure 1, the pipe is parameterized with length $L = 10D$ and diameter $D = 1$ m. It is initially conveying light fluid. Then, a stratified flow with two fluid layers is imposed at the inlet. The density and dynamic viscosity of the light fluid is $\rho_1 = 1$ kg m^{-3} and $\mu_1 = 0.005$ kg m s^{-1}. The density and dynamic viscosity ratios between two fluids are $\rho_2/\rho_1 = 5$ and $\mu_2/\mu_1 = 2$, respectively. The two fluids are immiscible. The boundary conditions are as follows: for the velocity, we assume a Dirichlet condition on the boundary and Neumann at the outflow. A specified velocity profile is imposed at the inlet, such as parabolic or uniform profile. On the pipe walls, the no-slip boundary condition is used. In terms of the phase field, the contact-angle boundary conditions are imposed on the pipe walls and outlet. The contact-angle boundary condition is governed by:

$$\boldsymbol{n} \cdot \nabla \left[\nabla^2 \phi \right] = 0, \quad \text{on } \partial \Omega, \tag{2.2a}$$

$$\boldsymbol{n} \cdot \nabla \phi = 0, \quad \text{on } \partial \Omega, \tag{2.2b}$$

where we assumed for simplicity that, if the fluid interface intersects the wall, the contact angle θ_s would be 90°. At the inlet, a Dirichlet condition is imposed for the phase field. The void fraction α_g denotes the volume of light fluid occupied when injecting it at the inlet. We use interface thickness $\eta = 0.005$ m, $\lambda \gamma_1 = 10^{-6}$, surface tension $\sigma = 0.001$ kg s^{-2} and gravity $g = 1$ m s^{-2} pointing downwards.

2.3. *Verification through convergence test*

A grid convergence with four mesh resolutions was conducted for two-phase flow simulation in an upward inclined two-dimensional conducting pipe with an inflow condition of $u = 1 - 4y^2$ and $\phi = -\tanh((y - 0.3)/\eta)$. Results for four grids, with [60 × 15], [60 × 20], [75 × 25] and [90 × 30] quad elements, were compared. Polynomial order $p = 5$ is used for all meshes. Figure 2 shows the time history of $\|U\|$ and $\|V\|$, the L2 norm of the velocity components in the whole fluid domain, defined as $\|U\| = \sqrt{\sum_\Omega u_i(x)}$. Table 1 shows the corresponding statistical information. The trends in the results are similar as we vary the mesh size. Furthermore, we also compare the temporal evolution of two fluids inside the channel at various time instants with four various resolutions. It is found that in all simulations, the two-phase flow transitions are similar, where an oscillating jet accompanied by vortex street formation is found; also a back flow develops that induces multiple rolling waves which interact with the jet. Therefore, in the rest of the paper we employ the second mesh size and fifth-order elements to balance computation cost and resolution accuracy.
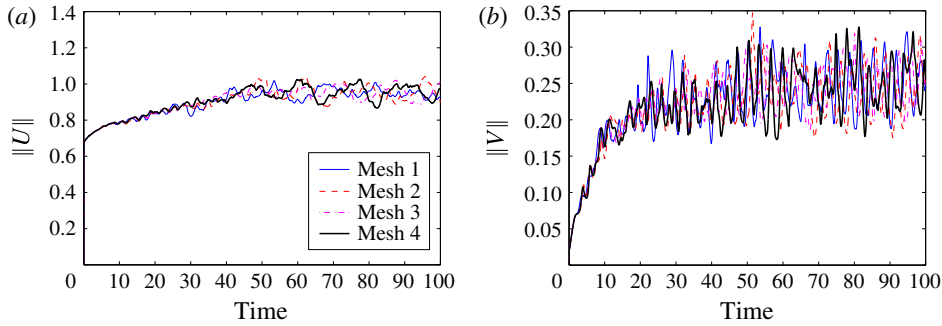
FIGURE 2. (Colour online) Time history of fluid velocity components $\|U\|$ and $\|V\|$ in the whole domain, for four different meshes. First mesh grid with $[60 \times 15]$ elements, second mesh grid with $[60 \times 20]$ elements, third mesh grid with $[25 \times 75]$ elements and fourth mesh grid with $[30 \times 90]$ elements. In all simulations the polynomial order is $p = 5$. The heavy fluid is placed at the top of the inlet.

Mesh	Mean($\|U\|$)	Root mean square($\|U\|$)	Mean($\|V\|$)	Root mean square($\|V\|$)
Mesh1	0.9407	0.0259	0.2423	0.0332
Mesh2	0.9431	0.0440	0.2377	0.0335
Mesh3	0.9473	0.0376	0.2424	0.0278
Mesh4	0.9483	0.0415	0.2398	0.0344

TABLE 1. Statistical information of figure 2.

2.4. *Validation for different flow regimes*

We validated the accuracy of phase-field approach in characterizing the two-phase flow regimes in a pipe, by conducting four DNS for a horizontal pipe and compared the results against the theoretical model of Taitel & Dukler (1976).

The flow regime map according to theory can be divided into four regions, including stratified flow, slug flow, dispersed bubble flow and annular flow; see figure 3. The triangle dots denote the bifurcations between various flow regimes. Here, the superficial velocity U^S for the light fluid (G) and heavy fluid (L) has been plotted along the horizontal and vertical axes, respectively. It is defined as $U_G^S = U_g * \alpha_g$, where U_g is the average velocity of the light fluid. Therefore, U_G^S can be regarded as the average velocity referenced with respect to the light fluid. Four cases, denoted by square points in the map are further simulated by the current phase-field approach. We confirmed that our method can characterize the flow regimes, as predicted by the Taitel & Dukler (1976) model, in both 2-D and 3-D simulations; see figures 4 and 5. The only exception is the annular flow pattern that can only exist in 3-D simulations.

More specifically, at very low superficial velocities the flow is stratified; see case 1 with $U_G^S = 0.7$, $U_L^S = 0.06$. As the heavy fluid rate U_L^S increases, the heavy fluid level rises and a surface wave can form. When the heavy fluid reaches the top of the pipe and blocks the entire cross-section, a slug is formed; see case 2 with $U_G^S = 0.25$, $U_L^S = 2$. At a higher heavy fluid rate, the equilibrium level of the heavy fluid approaches the top of the pipe. Therefore, the light fluid is mixed with the heavy fluid, and a dispersed bubble flow emerges; see case 3 with $U_G^S = 0.05$, $U_L^S = 8$. On the other hand, at higher light fluid rates, there is insufficient heavy fluid and the
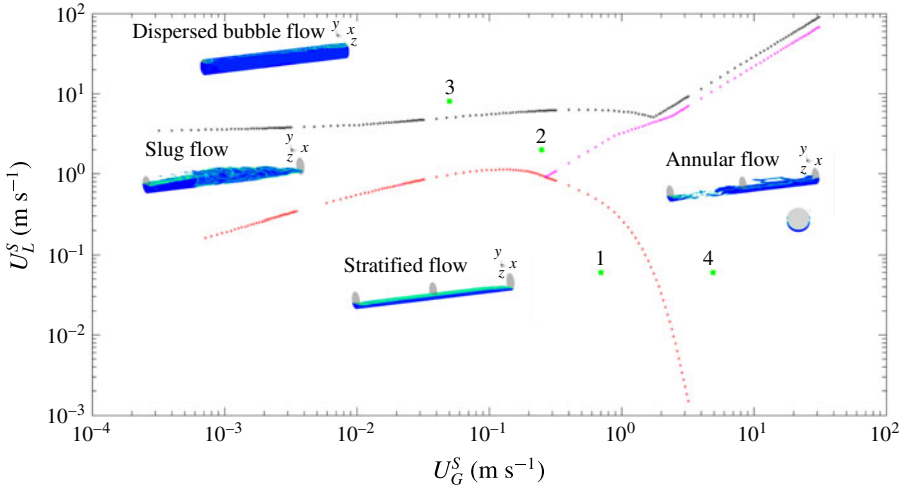
FIGURE 3. (Colour online) Flow regime map for a horizontal pipe, based on Taitel &
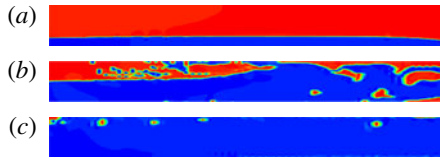Dukler (1976). Four DNS are shown at various flow conditions, denoted cases 1–4.

FIGURE 4. (Colour online) Various flow regimes in a 2-D horizontal pipe, corresponding
to cases 1–3 in figure 3. Case 1: $U_G^S = 0.7$, $U_L^S = 0.06$; case 2: $U_G^S = 0.25$, $U_L^S = 2$; case 3:
$U_G^S = 0.05$, $U_L^S = 8$. Blue colour denotes heavy fluid while red is used for the light fluid.

heavy fluid is swept up and around the pipe to form an annulus; see case 4 with
$U_G^S = 4.9$, $U_L^S = 0.06$ for the wavy annular flow pattern.

   Furthermore, a flow regime map for the inclined pipe ($\theta = 30°$) is shown in figure 6
using the theoretical model of Shoham (2006), since the model by Taitel & Dukler
(1976) can only be used up to 10° inclination. We see that the effect of inclination is
very pronounced, since the stratified flow regime disappears and the intermittent flow
(slug) takes place over a much wider range of flow conditions. Moreover, compared
to a horizontal pipe, the transition from slug flow to annular flow occurs at a lower
light fluid rate. Correspondingly, we perform three DNS at various flow conditions to
confirm the prediction of slug flow, wavy annular flow and dispersed bubble flow. The
simulation results are embedded into the flow regime map; they are similar to those
we see in figure 5.

   In the following, we focus on case 1 with $U_G^S = 0.5973$, $U_L^S = 0.069$ for the inclined
pipe, where the slug flow has formed. Usually, a stratified flow with heavy fluid in
the bottom layer is considered as the initial condition. However, in applications, if
the inclined section is connected to other sections, the inflow condition may vary.
Therefore, both 2-D and 3-D simulations will be conducted to investigate the flow
transition under various inflow arrangements between the light fluid and the heavy
fluid. We will also study the instability mechanisms of slug formation by analysing
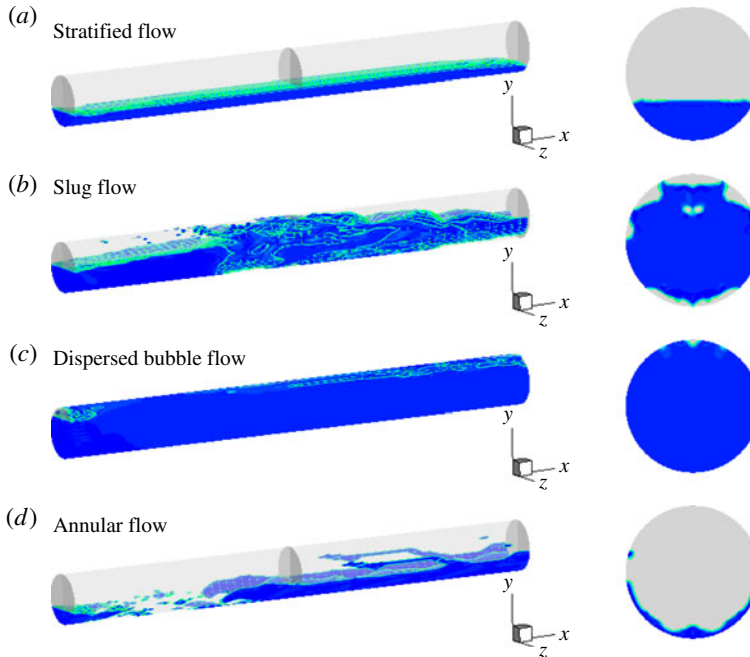the vorticity generation and circulation dynamics.

FIGURE 5. (Colour online) Various flow regimes in a horizontal pipe, corresponding to cases 1–4 in figure 3. Case 1: $U_G^S = 0.7$, $U_L^S = 0.06$; case 2: $U_G^S = 0.25$, $U_L^S = 2$; case 3: $U_G^S = 0.05$, $U_L^S = 8$; case 4: $U_G^S = 4.9$, $U_L^S = 0.06$. Only the heavy fluid is shown in blue.
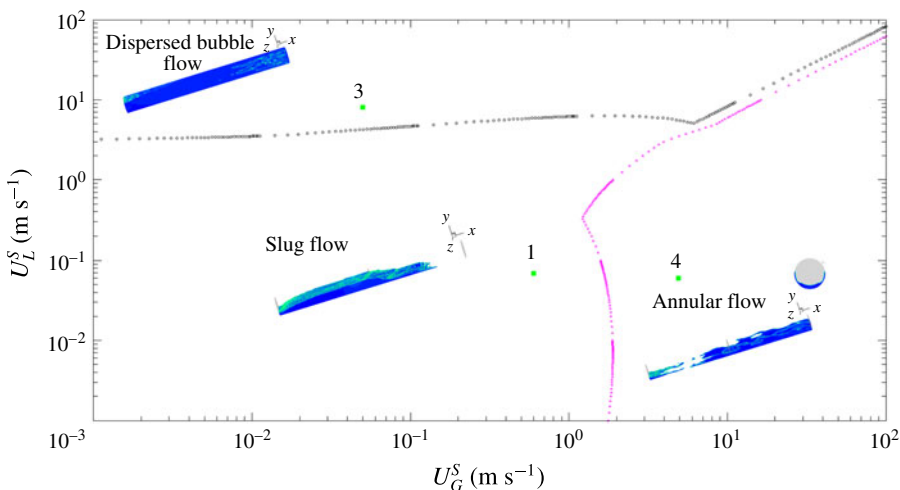

FIGURE 6. (Colour online) Flow regime map in the inclined pipe ($\theta = 30°$) based on the theoretical model of Shoham (2006). Three DNS are conducted at various flow conditions, denoted cases 1, 3, 4.

3. Two-phase flow in a 2-D upward inclined channel

In this section, we provide an overview of two-phase flow transition and the emergence of coherent vortices within a 2-D upward inclined channel. The important
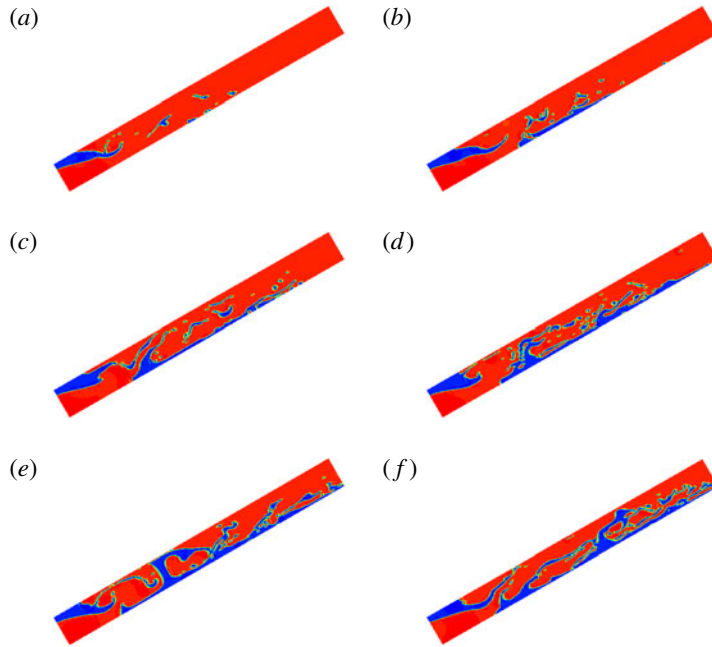
FIGURE 7. (Colour online) Temporal sequence of snapshots of two-phase flow patterns in a 2-D upward inclined channel at $\theta = 30°$. The time instants are (*a*) $t = 10$ s, (*b*) $t = 20$ s, (*c*) $t = 30$ s, (*d*) $t = 40$ s, (*e*) $t = 50$ s, (*f*) $t = 60$ s. At the inlet the heavy fluid is placed at the top layer. Blue colour stands for the heavy fluid while red stands for the light fluid. See supplementary movie 1 available at https://doi.org/10.1017/jfm.2017.417.

questions we will address are how vorticity reorganizes and what is the shape of the forming patterns.

3.1. *Heavy fluid on the top layer*

We first conduct simulations with the heavy fluid placed at the top layer at the inlet, with the inflow condition of $u = 1-4y^2$ and $\phi = -\tanh((y - 0.3)/\eta)$. Figure 7 shows the temporal evolution of two fluids inside the channel at various time instants: (*a*) $t = 10$ s, (*b*) $t = 20$ s, (*c*) $t = 30$ s, (*d*) $t = 40$ s, (*e*) $t = 50$ s, (*f*) $t = 60$ s. Blue colour stands for the heavy liquid while red stands for the light fluid. We find that an oscillating heavy liquid jet emerges first, which periodically hits the bottom wall as it develops further downstream. Subsequently, this heavy liquid jet stays aligned with the bottom wall, slowly flowing downward along the channel. When this layer of heavy fluid flows back to a certain location, it encounters a stagnation point area, when the back flow starts recirculating parallel to the heavy liquid jet and induces multiple rolling waves along its axis. Occasionally, a rolling wave can reach the top surface of the channel and forms a slug, e.g. at time $t = 50$ s, which blocks the entire channel section.

We also present the temporal sequence of vorticity contours ($-5 \leqslant \omega_z \leqslant 5$) in figure 8. The black line denotes the interface between the two fluids. It is found that the oscillating heavy liquid jet induces the formation of a vortex street-like flow along the channel axis. Along the direction of the jet, positive vortices form at its lower edge, which induce the roll up of negative vortices emanating from the bottom wall.
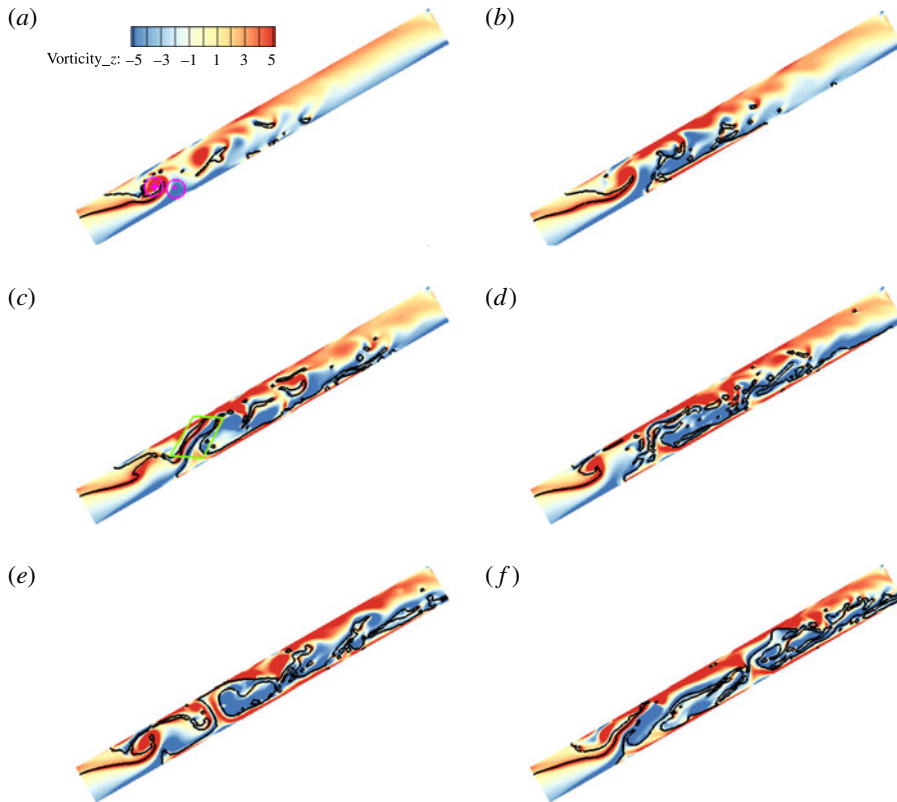
FIGURE 8. (Colour online) Temporal sequence of vorticity contours for two-phase flow in a 2-D upward inclined channel at $\theta = 30°$. The time instants are (*a*) $t = 10$ s, (*b*) $t = 20$ s, (*c*) $t = 30$ s, (*d*) $t = 40$ s, (*e*) $t = 50$ s, (*f*) $t = 60$ s. At the inlet the heavy fluid is placed at the top. Note that in this figure colours denote vorticity intensity and should not be confused with the colours denoting heavy and light fluid as in the previous figure. See movie 2.

In the area adjacent to the top edge of the jet, cross-annihilation is noted between opposite-signed vorticity, coming from the upper jet edge and the top wall. Back flow on the bottom wall induces the generation of positive vorticity. With the onset of rolling waves, negative vorticity is induced on the upper edge of the jet, while positive vorticity emerges on the lower edge. Consequently, the negative vorticity coming from the rolling waves will interact with previously formed positive vorticity from the jet. As the two come in contact, they disintegrate. This repeatable formation of vorticity and subsequent disintegration and crushing of the jet inside the channel causes a complex structure of the vorticity field in the middle section of the channel.

3.2. *Heavy fluid at the bottom layer*

When the heavy fluid is injected into the channel as the bottom layer, with the inflow condition of $u = 1 - 4y^2$ and $\phi = \tanh((y + 0.3)/\eta)$, it accumulates and forms a large slug, see figure 9. Next, this slug becomes unstable and the front part of it is injected forward, eventually coming into contact with the bottom surface of the channel wall; a part of the heavy fluid accumulates and then flows back toward the inlet, inducing
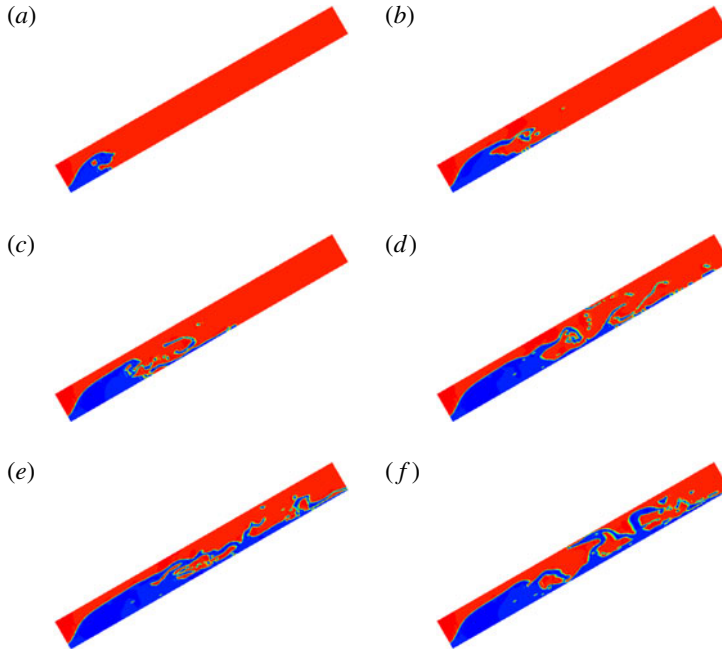
FIGURE 9. (Colour online) Temporal sequence of snapshots of two-phase flow pattern in a 2-D upward inclined channel $\theta = 30°$. The time instants are (*a*) $t = 10$ s, (*b*) $t = 20$ s, (*c*) $t = 30$ s, (*d*) $t = 50$ s, (*e*) $t = 70$ s, (*f*) $t = 183$ s. At the inlet the heavy fluid is placed at the bottom. Blue stands for the heavy liquid while red stands for the light fluid. See movie 3.

rolling waves. As in the previous case, a rolling wave can form another slug when it touches the top of channel, e.g. at $t = 183$ s.

In terms of vorticity contours, as shown in figure 10, with the formation of the slug negative vorticity emerges at the slug's top surface, while the positive vorticity on the top wall is enhanced, see $t = 10$ s. As the slug develops, pairs of vortices (denoted with circles) will develop and grow along the channel axis, see $t = 20$ s. As in the previous case, with heavy fluid at the top, the back flow produces positive vorticity on the bottom wall, which is not continuous along the wall, because of intermittently shed opposite vorticity caused by the rolling waves.

3.3. *Vorticity generation*

Above, we presented the development of two-phase flow in terms of the vorticity field inside an upward inclined channel. To quantitatively assess the generation of vorticity from two-phase interfaces, and from the channel walls, the circulation is calculated using Stokes' theorem and numerical integration:

$$\Gamma = \iint_A \omega_z(t)\, \mathrm{d}A, \tag{3.1}$$

where A is a measurement window inside the 2-D channel and ω_z is the vorticity component in the z direction. Four measurement windows are used in the current study, see figure 11. First, the channel domain is divided into 20 equal subsections
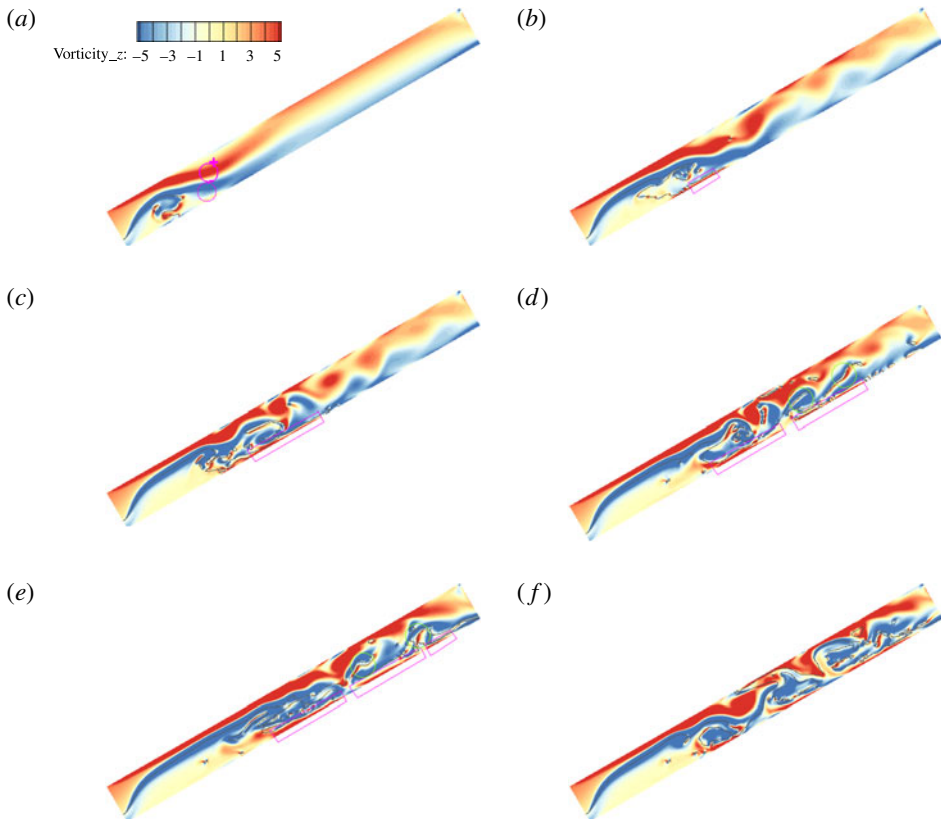
FIGURE 10. (Colour online) Temporal sequence of vorticity contour for two-phase flow in a 2-D upward inclined channel $\theta = 30°$. The time instants are (*a*) $t = 10$ s, (*b*) $t = 20$ s, (*c*) $t = 30$ s, (*d*) $t = 50$ s, (*e*) $t = 70$ s, (*f*) $t = 183$ s. At the inlet the heavy fluid is placed at the bottom. See movie 4.

along the axis. Within each subsection, we have $i/2 \leqslant x \leqslant (i+1)/2$, with $i = 0 : 19$. Then $A1_i$ denotes the region in the middle of the channel for various subsections along the axis, with the integration taking place over $-0.3 \leqslant y \leqslant 0.3$. Similarly, $A2_i$ and $A3_i$ denote the regions close to the top and bottom wall, respectively, corresponding to integration over $0.4 \leqslant y \leqslant 0.5$ and $-0.5 \leqslant y \leqslant -0.4$ for various subsections. Finally, $A4_i$ denotes the region across the entire channel subsection, with integration over $-0.5 \leqslant y \leqslant 0.5$. Here x, y are the non-dimensional coordinates along and perpendicular to the channel axis.

Figure 12 shows the temporal evolution of circulation within various measurement windows along the channel axis for the case with the heavy fluid placed as the top layer in the inlet. If we isolate a slice at any axial position, we can observe the change of circulation with time by the variation of the colour. Figure 13 shows the time history of circulations at different windows along the channel axis: 1, 2, 4, 7.

We find that $x = 2$ is a critical position, as it corresponds to the stagnation point of the back flow on the bottom wall. Specifically, the net circulation around $A4$ is positive in subsection $x < 2$; we find that the amount of positive circulation produced by the unstable oscillating jet flow in figure 7 is higher than that of negative circulation generated from the top and bottom wall surfaces. However, in the subsection $x \geqslant 2$, the circulation fluctuates as the vortex shedding becomes erratic
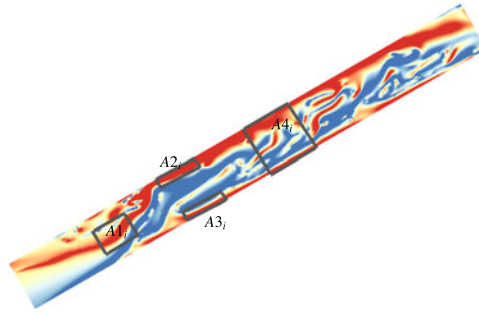
FIGURE 11. (Colour online) Sketch of four typical measurement windows $A1_i$–$A4_i$ along the channel axis over which the vorticity balance is computed. $A1_i$–$A4_i$ with $i = 0:19$ are within 20 equal subsections along the axis.
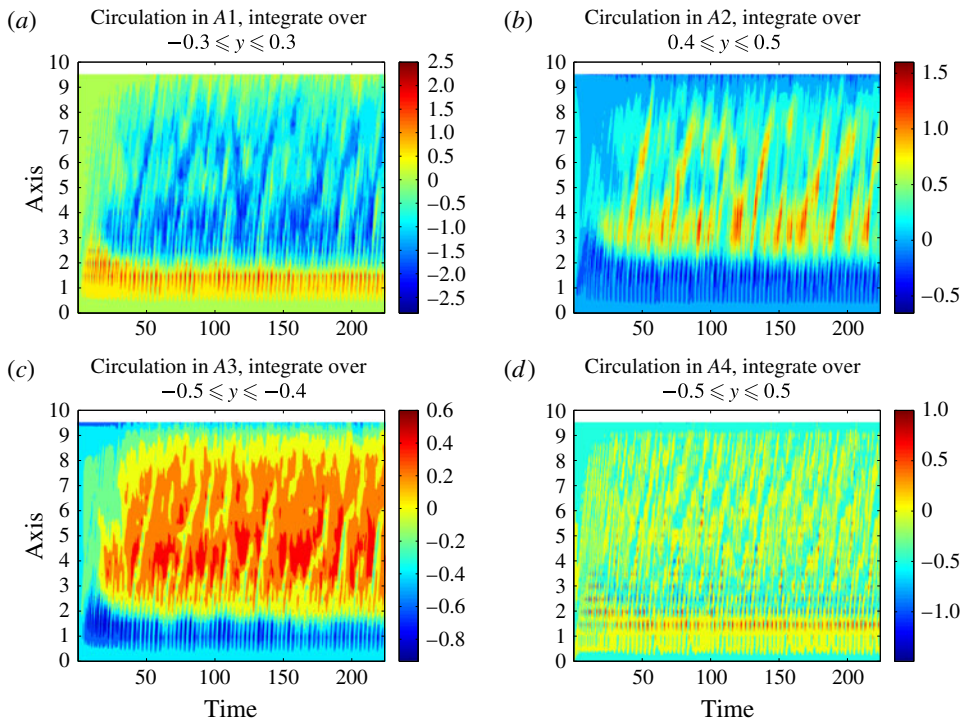

FIGURE 12. (Colour online) Temporal evolution of circulations at different windows along the channel axis. (*a*) $A1$, (*b*) $A2$, (*c*) $A3$ and (*d*) $A4$. The heavy fluid is placed at the top of the inlet.

along the channel axis. In the top wall region $A2$, a positive circulation is observed at $x \geqslant 2$, occasionally increasing in intensity due to the interaction of vorticity shed from the jet. In the middle region $A1$, a negative circulation is seen at $x \geqslant 2$, a combination of vorticity generated from the messy shedding of the jet and the rolling waves of back flow. Furthermore, on the bottom wall region $A3$, the back flow continuously induces positive circulation.

Similarly, we analyse the circulation dynamics when the heavy fluid is injected as the bottom layer in the inlet; see figure 14. The heavy liquid slug reaches a quasi-
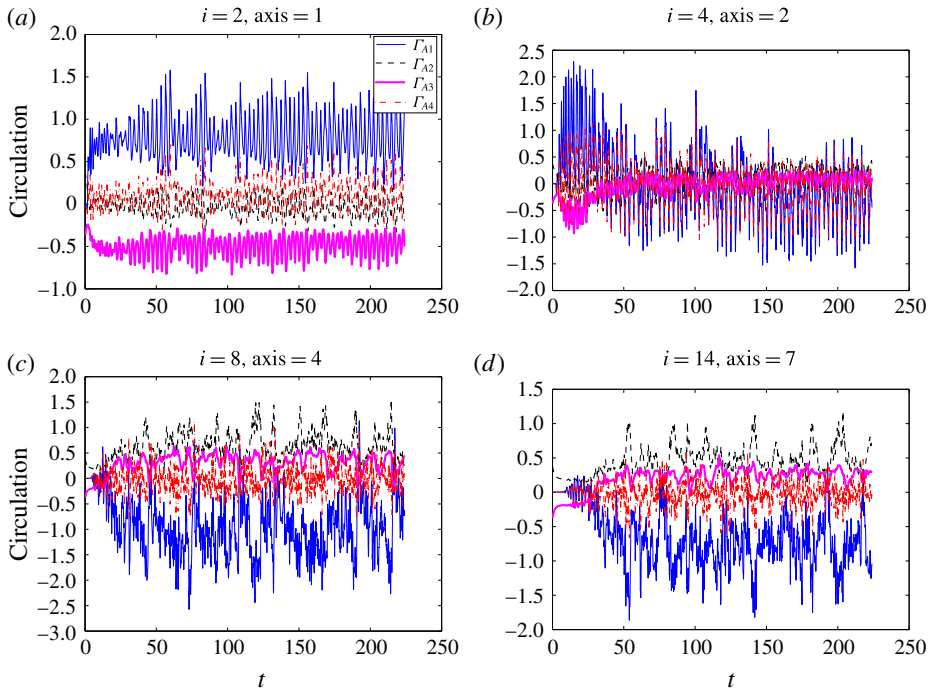
FIGURE 13. (Colour online) Time history of circulation at different windows along the channel axis: 1, 2, 4, 7. The heavy fluid is placed at the top of the inlet.

steady state after $t = 45$ s. Specifically, at $x \leqslant 2$, the circulation is negative in the middle region ($A1$), corresponding to the initially formed heavy fluid slug and the generation of negative vorticity from its top interface. Meanwhile, the circulation at $x \leqslant 2$ near the top wall region ($A2$) is almost equal to that in the middle region ($A1$). On the bottom wall region ($A3$), the circulation is almost zero at $x \leqslant 2$ due to the cross-annihilation of opposite-sign vorticity generated between the right surface of the slug and the bottom wall of channel. At the subsections with $2 \leqslant x \leqslant 3$, the circulation ($\Gamma_1$) starts oscillating as function of time, corresponding to the unstable vortex shedding in figure figure 10. At the subsections with $4 \leqslant x \leqslant 6$, intermittent behaviour is seen for the circulation in both the ($A1$) and ($A2$) regions, which corresponds to the irregular crushing of the heavy liquid slug on the right surface and its interaction with the vortex shedding from the top wall. However, at the subsections with $6 \leqslant x \leqslant 8.5$, the circulation fluctuates randomly in the region ($A1$), due to contribution of negative circulation from the unsteady rolling waves. Nevertheless, near the bottom wall region ($A3$), positive circulation is found due to vorticity generation from the back flow along the bottom wall.

In summary, in both cases, the net circulation on the entire channel section ($A4$) shows that the vorticity generated from the two-phase flow interfaces and the channel walls is generally negative, while positive vorticity is contributed by the oscillating jet and the back flow inside the inclined pipe.

3.4. *Comparison against the horizontal channel*

In this subsection we study the effect of the inclination angle on the two-phase flow mechanisms inside the channel when the heavy fluid is the top layer. In figure 15,
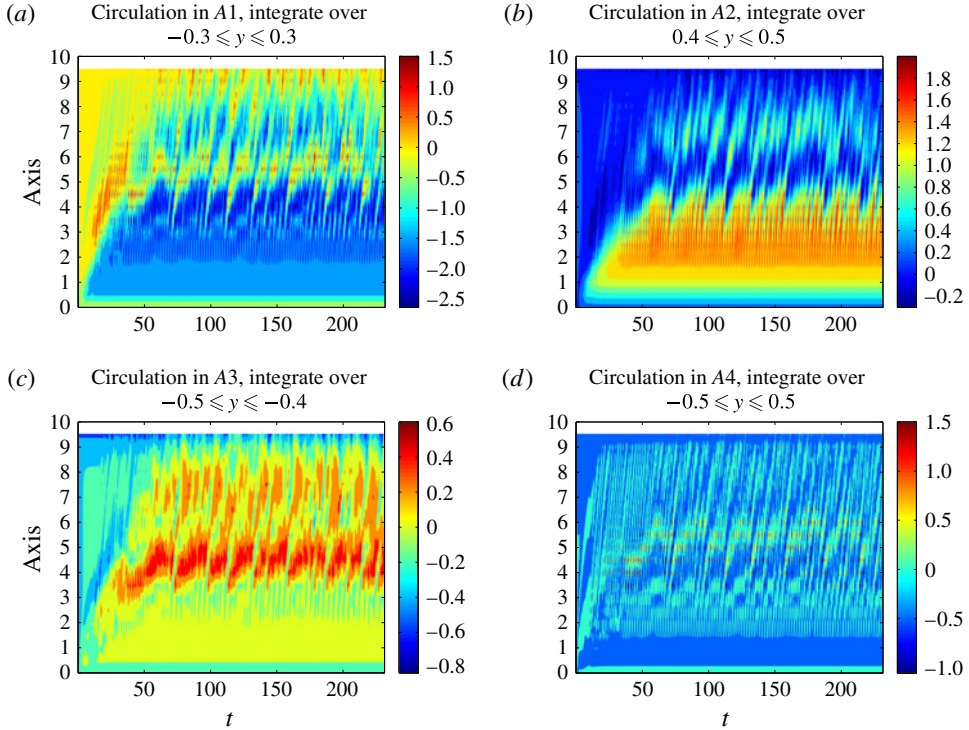
FIGURE 14. (Colour online) Temporal evolution of circulation within various measurement windows along the channel axis. (*a*) *A*1, (*b*) *A*2, (*c*) *A*3 and (*d*) *A*4. The heavy fluid is placed at the bottom of the inlet.
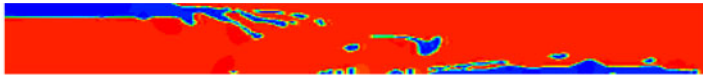

FIGURE 15. (Colour online) Instantaneous two-phase flow pattern in a 2-D horizontal channel. At the inlet, the heavy liquid is placed as the top layer. Blue colour stands for the heavy fluid while red stands for the light liquid.

we have found that, due to the gravity effect, the injected heavy fluid accumulates on the bottom wall of the horizontal channel. As the flow develops, the heavy fluid layer moves to the exit of the channel smoothly. For the inclined channel, we no more observe the back flow or the rolling waves, as shown in figure 7.

As shown in § 2.4, a stratified flow is induced in the horizontal channel. We show here that when the heavy fluid is placed as the top layer, an unsteady flow transition is obtained in the upstream part of the channel, while a stratified wavy flow can still be found in the downstream part of the channel.

4. Two-phase flow in a 3-D upward inclined pipe

In this section, we perform three-dimensional simulations of two-phase flow in a circular inclined pipe, under similar inflow conditions as for § 3, with velocity profile: $u = 1 - 4(y^2 + z^2)$. Three-dimensional flow transition and circulation dynamics are discussed.
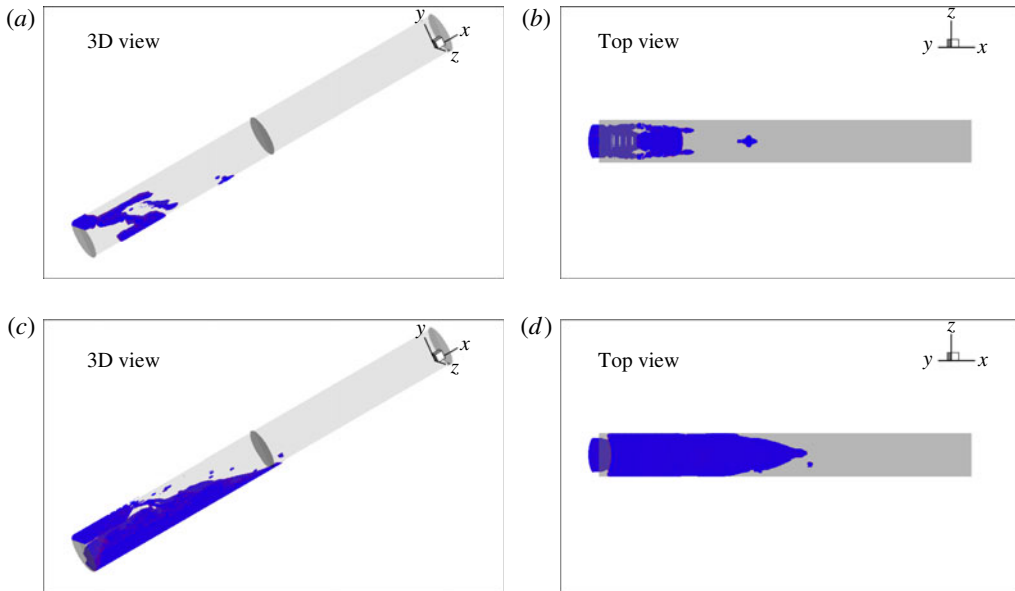
FIGURE 16. (Colour online) Two instantaneous two-phase flow patterns in a 3-D upward inclined pipe for $\theta = 30°$. (*a,b*) $t = 5$ s; (*c,d*) $t = 60$ s. At the inlet, the heavy fluid is placed as the top layer. Blue colour stands for the heavy fluid.
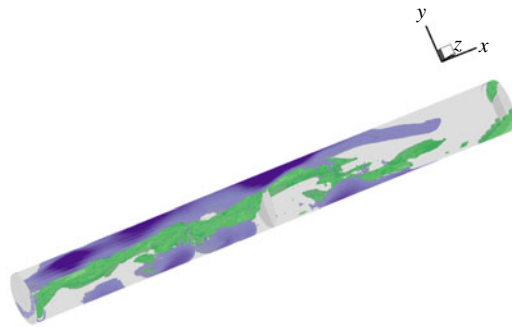

FIGURE 17. (Colour online) Instantaneous vorticity contours (ω_z) for two-phase flow in a 3-D upward inclined pipe with $\theta = 30°$. Purple colour stands for $\omega_z \geqslant 4$ while green stands for $\omega_z \leqslant -4.5$. At the inlet, the heavy fluid is placed as the top layer.

Two instantaneous two-phase flow patterns are shown in figure 16 when the heavy fluid is the top layer, with ϕ profile: $\phi = -\tanh((y - 0.3)/\eta)$. To characterize the 3-D patterns, only the heavy fluid is shown in blue colour. It is seen that the injected heavy fluid forms two symmetric jets, connected by rings at the inlet region. Subsequently, parts of the jets hit the bottom wall of the circular pipe, and then slowly flow downwards along the pipe. As time progresses, the heavy fluid forms a large slug on the bottom wall. After some heavy liquid accumulation, the slug develops intense unstable motion at its top interface because the jet flow interacts with the slug instead
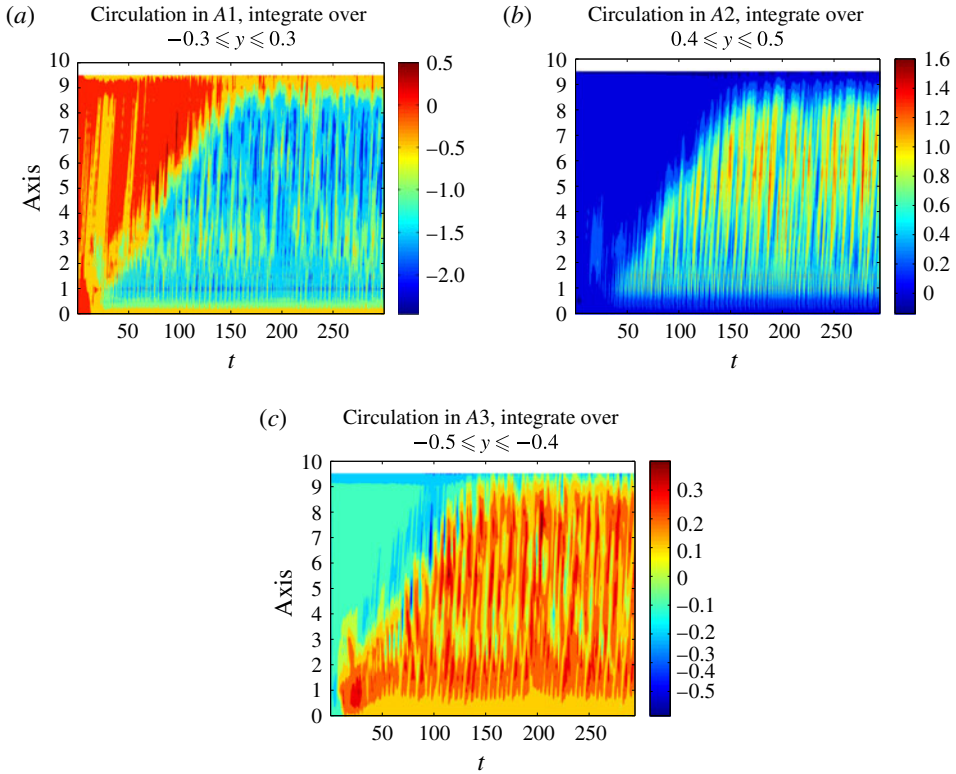
(*a*) Circulation in *A*1, integrate over −0.3 ⩽ *y* ⩽ 0.3

(*b*) Circulation in *A*2, integrate over 0.4 ⩽ *y* ⩽ 0.5

(*c*) Circulation in *A*3, integrate over −0.5 ⩽ *y* ⩽ −0.4

FIGURE 18. (Colour online) Temporal evolution of circulation in window *A*1, *A*2, *A*3 for two-phase flow in a 3-D upward inclined pipe with $\theta = 30°$. The heavy fluid is placed as the top layer at the inlet.

of the bottom wall. Meanwhile, part of the slug starts rolling up into waves as it further develops upwards along the pipe. From the instantaneous vorticity contours ω_z in figure 17, it is seen that the unstable slug will induce negative vorticity at its top surface, while positive vorticity on the top wall is enhanced. The back flow in the slug generates positive vorticity, while vorticity discontinuities correspond to the occurrence of multiple rolling waves in the slug.

In terms of circulation generation, earlier we focused on integrating ω_z in four measurement windows, as shown in figure 11. However, for the circular pipe, the measurement windows are taken on a thin layer with $-0.05 \leqslant z \leqslant 0.05$ and the average circulation is calculated. We find that there are similarities and differences between the flow mechanisms in a circular pipe and those in a two-dimensional channel. In particular, we find differences in the generation of vorticity in a circular pipe versus that observed in the 2-D case. As seen in figure 18, in both the *A*2 and *A*3 regions a positive circulation is found, and negative circulation is obtained only in the middle area of the pipe, *A*1. In the 2-D case, this applies only to the part between $x/D = 3$ to 8 along the axis, while between $x/D = 0$ to 2 the jet rings dominate the vorticity generation causing positive circulation in *A*1 and negative circulation in the *A*2 and *A*3 regions; this is not observed in the 3-D circular pipe case.

Figure 19 presents the instantaneous two-phase flow patterns in a 3-D upward inclined pipe when the heavy fluid is as the bottom layer, with ϕ profile: $\phi =$
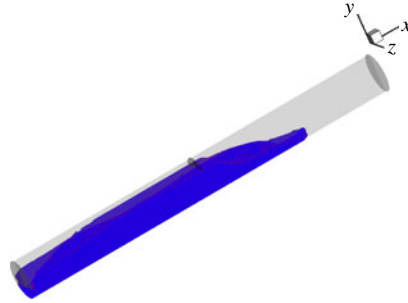
FIGURE 19. (Colour online) Instantaneous two-phase flow pattern in a 3-D upward inclined pipe with $\theta = 30°$. At the inlet, the heavy fluid is placed as the bottom layer. Colour blue stands for the heavy fluid.
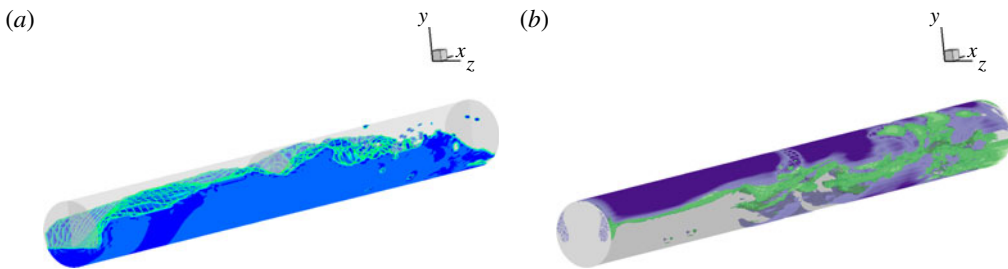

FIGURE 20. (Colour online) Instantaneous phase field and vorticity contours for two-phase flow in a 3-D upward inclined pipe for $\theta = 30°$. (*a*) Two-phase flow pattern. (*b*) Cross-flow vorticity component ω_z; purple colour stands for $\omega_z \geqslant 4$ while green stands for $\omega_z \leqslant -4.5$. $Re = 1500$.

$\tanh((y + 0.3)/\eta)$. We see that a large heavy fluid slug smoothly forms and slowly fills up the lower half of the circular pipe. The leading surface of the slug is more flat than at other positions. Compared to the previous 2-D case with heavy fluid at the bottom, the flow transition in a 3-D circular pipe is more stable. Both the instability of the slug at the leading edge and the back flow inside the slug are so weak that they cannot disrupt the flow transition in the upstream part of the pipe. However, as the Reynolds number increases, we find that an unstable slug can form; see figure 20 for $Re = 1500$, where the upstream side of the slug moves erratically while waves are induced. We note that an entropy–viscosity-based LES method (Guermond, Pasquetti & Popov 2011) is used to simulate the high Reynolds number flow inside the pipe.

5. Conclusions

In this paper, the phase-field approach is firstly validated against the theoretical models of Taitel & Dukler (1976), Shoham (2006), which predict the various flow regimes for horizontal and inclined pipes transporting two-phase flow. These regimes that include stratified flow, slug flow, dispersed bubble flow and annular flow, have all been identified and studied in our DNS. Then, the instability mechanisms of slug flow formation in an inclined pipe are investigated by analysing two-phase flow patterns and the associated vorticity dynamics. When the heavy fluid is injected as the bottom layer, the formation and unstable evolution of a slug is observed in 2-D simulations.

When the heavy fluid is placed at the top, an oscillating jet with vortex street formation is captured. In both cases, a back flow results that induces multiple rolling waves, and which further interact with the slug or jet, complicating the flow transition. The vorticity dynamics is similar in both cases in terms of the net circulation of the entire channel section (*A*4), showing that negative vorticity generation results from two-phase flow interfaces and the channel walls, while positive vorticity components are caused by the oscillating jet and the back flow inside the inclined pipe.

Finally, through 3-D simulation of flow in a circular pipe, it is found that the two-phase flow becomes stable when the heavy fluid is injected as the bottom layer, but a slug instability develops for higher Reynolds numbers. When the heavy fluid is injected as the top layer, 3-D vortex rings are induced in the circular pipe, instead of the 2-D periodical vortex formation. Overall, the vorticity generation and circulation dynamics in a circular pipe are slight different from those we observe for a 2-D channel flow.

Supplementary movies

Supplementary movies are available at https://doi.org/10.1017/jfm.2017.417.

REFERENCES

BARNEA, D. & TAITEL, Y. 1993 A model for slug length distribution in gas–liquid slug flow. *Intl J. Multiphase Flow* **19** (5), 829–838.

BATCHELOR, G. K. 2000 *An Introduction to Fluid Dynamics*. Cambridge University Press.

BENDIKSEN, K., MALNES, D., STRAUME, T. & HEDNE, P. 1990 A non-diffusive numerical model for transient simulation of oil–gas transportation systems. In *Proc. 1990 European Simulation Multiconference*, pp. 508–515. SCS Europe.

BRATLAND, O. 2010 *Pipe Flow 2: Multi-phase Flow Assurance* http://www.drbratland.com/.

BRØNS, M., THOMPSON, M. C., LEWEKE, T. & HOURIGAN, K. 2014 Vorticity generation and conservation for two-dimensional interfaces and boundaries. *J. Fluid Mech.* **758**, 63–93.

BUNNER, B. & TRYGGVASON, G. 2002a Dynamics of homogeneous bubbly flows. Part 1. Rise velocity and microstructure of the bubbles. *J. Fluid Mech.* **466**, 17–52.

BUNNER, B. & TRYGGVASON, G. 2002b Dynamics of homogeneous bubbly flows. Part 2. Velocity fluctuations. *J. Fluid Mech.* **466**, 53–84.

CAMPBELL, B. K. 2015 A mechanistic investigation of nonlinear interfacial instabilities leading to slug formation in multiphase flows. PhD thesis, Massachusetts Institute of Technology.

DONG, S. & SHEN, J. 2012 A time-stepping scheme involving constant coefficient matrices for phase-field simulations of two-phase incompressible flows with large density ratios. *J. Comput. Phys.* **231** (17), 5788–5804.

DUKLER, A. E. & HUBBARD, M. G. 1975 A model for gas–liquid slug flow in horizontal and near horizontal tubes. *Ind. Engng Chem. Fundam.* **14** (4), 337–347.

ESMAEELI, A. & TRYGGVASON, G. 1998 Direct numerical simulations of bubbly flows. Part 1. Low reynolds number arrays. *J. Fluid Mech.* **377**, 313–345.

ESMAEELI, A. & TRYGGVASON, G. 1999 Direct numerical simulations of bubbly flows. Part 2. Moderate reynolds number arrays. *J. Fluid Mech.* **385**, 325–358.

FABRE, J. & LINÉ, A. 1992 Modeling of two-phase slug flow. *Annu. Rev. Fluid Mech.* **24** (1), 21–46.

GUERMOND, J.-L., PASQUETTI, R. & POPOV, B. 2011 Entropy viscosity method for nonlinear conservation laws. *J. Comput. Phys.* **230** (11), 4248–4267.

HIRT, C. W. & NICHOLS, B. D. 1981 Volume of fluid (vof) method for the dynamics of free boundaries. *J. Comput. Phys.* **39** (1), 201–225.

ISSA, R. I. & KEMPF, M. H. W. 2003 Simulation of slug flow in horizontal and nearly horizontal pipes with the two-fluid model. *Intl J. Multiphase Flow* **29** (1), 69–95.

KARNIADAKIS, G. E. & SHERWIN, S. J. 2013 *Spectral/hp Element Methods for Computational Fluid Dynamics*, 2nd edn. Oxford University Press.

MORTON, B. R. 1984 The generation and decay of vorticity. *Geophys. Astrophys. Fluid Dyn.* **28** (3–4), 277–308.

NAGRATH, S., JANSEN, K. E. & LAHEY, R. T. 2005 Computation of incompressible bubble dynamics with a stabilized finite element level set method. *Comput. Meth. Appl. Mech. Engng* **194** (42), 4565–4587.

ROSENHEAD, L. 1963 *Laminar Boundary Layers*. Clarendon Press.

SANCHEZ-SILVA, F., CARVAJAL-MARISCAL, I., TOLEDO-VELÁZQUEZ, M., LIBREROS, D. & SAIDANI-SCOTT, H. 2013 Experiments in a combined up stream downstream slug flow. In *EPJ Web of Conferences*, vol. 45, p. 01082. EDP Sciences.

SAUSEN, A., DE CAMPOS, M. & SAUSEN, P. 2012 *The Slug Flow Problem in Oil Industry and Pi Level Control*. INTECH Open Access Publisher.

SHOHAM, O. 2006 *Mechanistic Modeling of Gas–Liquid Two-Phase Flow in Pipes*, Society of Petroleum Engineers.

SUSSMAN, M., SMEREKA, P. & OSHER, S. 1994 A level set approach for computing solutions to incompressible two-phase flow. *J. Comput. Phys.* **114** (1), 146–159.

TAITEL, Y. & BARNEA, D. 1990 Two-phase slug flow. *Adv. Heat Transfer* **20**, 83–132.

TAITEL, Y. & DUKLER, A. E. 1976 A model for predicting flow regime transitions in horizontal and near horizontal gas–liquid flow. *AIChE J.* **22** (1), 47–55.

TRYGGVASON, G., BUNNER, B., ESMAEELI, A., JURIC, D., AL-RAWAHI, N., TAUBER, W., HAN, J., NAS, S. & JAN, Y. J. 2001 A front-tracking method for the computations of multiphase flow. *J. Comput. Phys.* **169** (2), 708–759.

YUE, P., FENG, J. J., LIU, C. & SHEN, J. 2004 A diffuse-interface method for simulating two-phase flows of complex fluids. *J. Fluid Mech.* **515**, 293–317.

ZHENG, G., BRILL, J. P. & TAITEL, Y. 1994 Slug flow behavior in a hilly terrain pipeline. *Intl. J. Multiphase Flow* **20** (1), 63–79.

ZHENG, X., BABAEE, H., DONG, S., CHRYSSOSTOMIDIS, C. & KARNIADAKIS, G. E. 2015 A phase-field method for 3d simulation of two-phase heat transfer. *Intl J. Heat Mass Transfer* **82**, 282–298.

ZHENG, X. & KARNIADAKIS, G. E. 2016 A phase-field/ale method for simulating fluid-structure interactions in two-phase flow. *Comput. Meth. Appl. Mech. Engnng* **309** (1), 19–40.